TRIBOLOGY TRANSACTIONS
2026, VOL. 69, NO. 2, 296–309
https://doi.org/10.1080/10402004.2025.2595444

stle
Society of Tribologists
and Lubrication Engineers

Influence of Micro-Structured Setter Plates on Friction During Sintering of Metal Binder Jetting Components

Heiko Blunk[a] and Arthur Seibel[b]

[a]Fraunhofer Research Institution for Additive Manufacturing Technologies IAPT, Hamburg, Germany; [b]Institute for Production Technology and Systems, Leuphana University Lüneburg, Lüneburg, Germany

ABSTRACT
Metal binder jetting (MBJ), an additive manufacturing process, enables the resource-efficient production of highly complex metal components and offers a cost advantage over metal injection molding, particularly for small batch sizes. At the end of the MBJ process, the components undergo sintering, during which they experience shrinkage of up to 20%. The relative movement between the component and the setter plate during this process induces stresses and undesired distortions caused by frictional forces. Reducing the coefficient of friction is identified as a potential solution to this problem. In this paper, the effect of micro-structured setter plates on friction during sintering is investigated. Eight different surface structures are fabricated and tested at ambient temperatures of 20 °C and 1,100 °C. The results indicate that friction increases due to the surface topography of the additively manufactured components in combination with insufficiently small structural elements. However, post-processing the surfaces led to a friction reduction of up to 34%.

ARTICLE HISTORY
Received 19 February 2025
Accepted 20 November 2025

KEYWORDS
Unlubricated friction;
surface modification;
surface roughness

Introduction

Additive manufacturing (AM) processes enable the efficient manufacturing of highly complex components, but their broader adoption is often limited by relatively high production costs. Compared to the established metal AM technologies, metal binder jetting (MBJ) offers significantly lower component costs, for example, up to 60% less than laser powder bed fusion for metals (PBF-LB/M). (*1*) Furthermore, compared to metal injection molding (MIM), MBJ allows for greater design complexity and improved cost efficiency at lower production volumes, as it eliminates the need for tooling. Shaping in MBJ involves a layer-by-layer selective deposition of binder onto a flat powder bed. After printing, the powder cake containing the components is cured in an oven and the parts are subsequently depowdered. Depending on process control, either thermal or catalytic debinding is then performed, followed by sintering of the components. The sintering process of the parts is carried out on ceramic setter plates. Once sintering is complete, the components can either be used directly or undergo conventional post-processing, if required. Nonetheless, the sintering process still faces certain challenges. For example, the combination of friction, gravity, and high temperatures can lead to undesirable deformation of the components. (*2*,*3*) To mitigate such effects, reducing friction during sintering becomes essential. Beyond conventional approaches like the use of lubricants, alternative methods such as structuring of surfaces exist to reduce friction. (*4*)

Structuring is a method for functionalizing surfaces, giving them dirt-repellent properties, changing their appearance, or influencing their tribological properties, for example. This involves selectively removing or adding volume elements from a surface to create the desired topography. A basic distinction can be made between defined and undefined surface structures. While the latter are created by means such as sandblasting and do not have a repeatable pattern, defined structures have a repeatable, describable pattern, which is usually the subject of investigations into surface structuring. These patterns can be produced, for example, by a laser beam ablation process. (*5*) Such surfaces are used in both dry and lubricated friction pairs to adjust the tribological properties. In both cases, the reduction in friction is assumed to be due to a reduction in the contact area, (*6*) whereby the effect is less pronounced in dry friction. (*7*,*8*) In addition, wear at the contact level is also reduced, as the gaps absorb wear particles and thus remove them from the contact zone. (*9*–*11*) In a review paper, Mao et al. (*12*) demonstrate the potential of surface structuring under dry conditions. Depending on the structure and material pairing, the coefficient of friction can be reduced by more than 50% or increased by more than 346%. Figure 1 shows an overview of selected typical surface structures

CONTACT Arthur Seibel arthur.seibel@leuphana.de
Review led by S. Kailas.

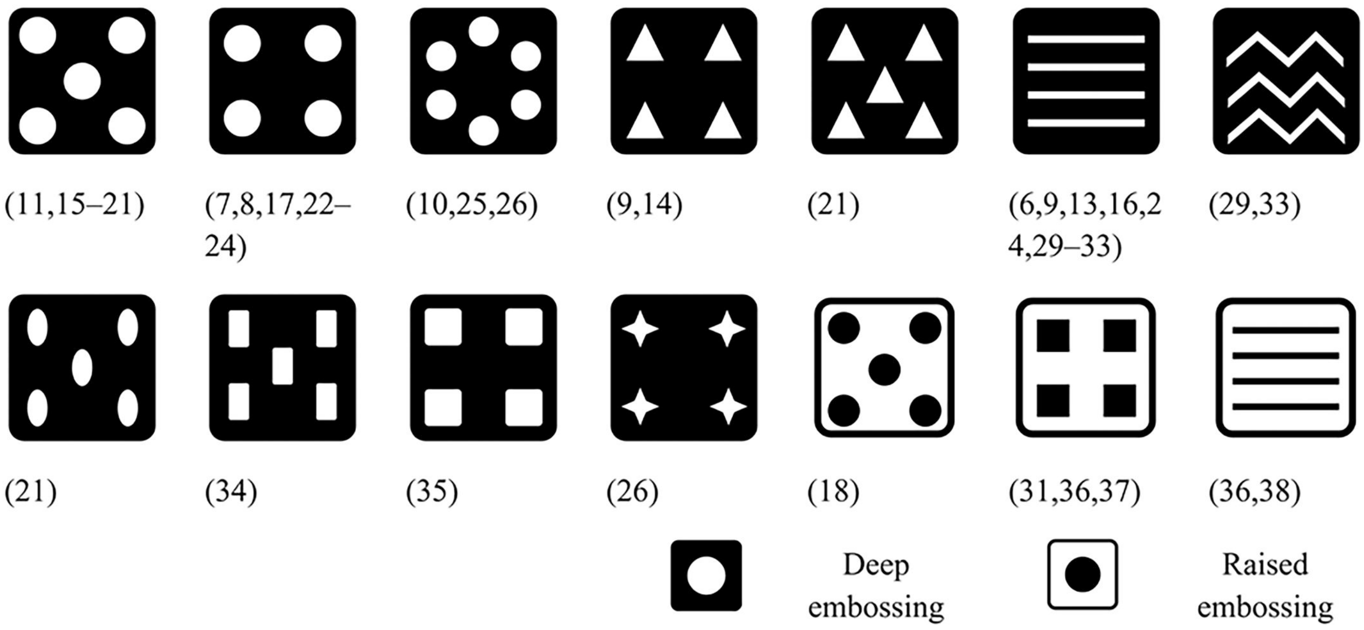

Figure 1. Overview of different surface structures and classification in terms of shape, arrangement, and characteristics.

used in the literature, including the structure type and arrangement. The size of the structures varies between 0.1 µm (*13*) and 500 µm (*14*) and is independent of the design of the structure. A basic distinction can be made between point-like and line-like structures. Most structures have a deep embossing and a point-like shape. These structures are usually circular in design. (*7*,*8*,*10*,*11*,*15–26*) Occasionally, other shapes such as ellipses, (*21*) triangles, (*9*,*14*,*21*) squares, (*27–31*) or stars (*26*) are also investigated. The arrangement is either square, hexagonal, or ring-shaped. In the case of linear structures, a distinction can be made between straight (*6*,*9*,*13*,*16*,*24*,*29*,*30*,*32–36*) and jagged lines. (*32*,*35*) Additionally, there are special shapes such as the combination of triangular and circular structural elements (*37*) or irregular structures. (*38*)

However, depending on the type and design of the structural elements, both friction asymmetry and friction anisotropy can occur. This means that the effect changes when the direction of movement is reversed, or the orientation of the movement relative to the structure is changed. For example, linear structures lead to an increase in the friction coefficient when aligned parallelly to the sliding direction and to a decrease when aligned transversely. (*13*,*33*) In order to achieve a direction-independent effect, a structure that is as isotropic as possible is therefore required. (*13*,*31*) There is no clear correlation regarding the size of the structural elements, as both larger and smaller structural elements can achieve a reduction in friction. However, structures that are too fine can increase friction, as this is accompanied by an increase in contact pressure around the structural elements. (*39*) The depth of the structures has already been identified as insignificant. (*8*,*40*) However, it should be noted that wear particles must continue to be absorbed, as otherwise there will no longer be any friction- and wear-reducing effect. (*26*) Although there are some conflicting statements regarding the surface area of the structures, most results show a greater reduction in friction with higher structure density. (*11*,*15*) Nevertheless, each contact situation requires its own structural elements, including its own shape, size, and density. (*21*)

Rosenkranz et al. (*41*) have formulated eight general recommendations that should be taken into account when designing surface structures:

1. The distance between structural elements should not be too large, as otherwise wear particles cannot be effectively removed.
2. In case of bore features, if the structural element density is too high, there is not enough surface area to absorb normal forces, or the load-bearing capacity of the contact surface is too low.
3. If the structural elements are too deep, stress peaks will lead to excessive plastic deformation.
4. Lower-lying areas of the structure must be able to accommodate even the largest wear particles that occur.
5. The manufacturing process used to produce the structure should induce as little internal stress as possible in the material.
6. The influence of the structure on properties that can indirectly affect wear and friction must be understood—in particular, heat transfer and surface energy.
7. Rationally designed textures, especially those determined with the aid of simulations, can be used to improve tribological performance.
8. Where possible, a structured surface should be used in combination with solid lubricants.

In summary, it can be said that despite the large number of structures of various sizes and shapes that have already been investigated, it is still not possible to systematically design and optimize the structure for a given application on the basis of the literature. (*40*) This includes not only the number and size of the structural elements, but also their shape and arrangement. In addition, the base and counter bodies used in previous studies have been manufactured conventionally. It is not yet known whether the friction reduction effect also applies to additively manufactured counter bodies.

In this paper, the influence of micro-structured setter plates on the friction behavior during the sintering process of MBJ components is investigated, making an original contribution to the field of sintering.

1. The first in situ measurements of static and dynamic friction during MBJ sintering (20 °C vs. 1,100 °C) are presented, obtained while parts shrink on setter plates that were equipped with deliberately engineered micro-textures.
2. By pairing these textures with both as-printed and ground MBJ coupons, the governing role of native, particle-induced surface roughness in the transition from adhesion- to form-fit-dominated friction is revealed.
3. Across eight pillar- and dimple-type patterns spanning contact-area ratios from 21% to 76%, the operating windows in which texturing lowers friction by up to 34%—and, conversely, the regimes in which certain textures amplify friction and part distortion—are identified.

The design parameters of these structures, such as feature size, are systematically varied to identify configurations that minimize frictional forces. In addition, a detailed analysis of the relationships between surface characteristics, such as roughness and topography, and their effects on the coefficients of friction at both room and elevated temperature of 1,100 °C is presented. Dilatometric tests have shown that there is sufficient sintering activity and component shrinkage at this temperature. These phenomena have consequently resulted in relative movement in relation to the setter plate. (*42*)

Surface structure

During sintering, the direction of movement of each volume element of a component can be aligned differently in the contact plane. If, for example, a line-like surface structure is applied, both an anisotropic and an asymmetric influence on the coefficients of friction occurs, depending on the design. (*13*,*33*) Another possibility, which has already been investigated, would be to arrange the structural elements in concentric rings. (*10*) However, this requires knowledge of the center of shrinkage of each component and its exact placement on the surface structure. To achieve a direction-independent effect, a structure that is as isotropic as possible is therefore required. (*13*,*31*) A commonly used and effective surface structure consists of cylindrical protrusions or blind holes (Fig. 2, left). (*10*,*11*,*21*,*22*,*26*) If these holes are arranged in a hexagonal pattern (Fig. 2, center), a high structural element density can be achieved. (*11*) Alternatively, a square arrangement (Fig. 2, right) may be used, though it results in a slightly lower maximum density of structural elements. For both arrangements, three design parameters define the structure, as illustrated in Fig. 2:

- h_S: structural height;
- d_S: structural element diameter;
- a_S: spacing between two structural elements.

Due to manufacturing limitations, it is not possible to create a planar drilling base, which is why for holes, the height h_S is defined as the maximum distance between the drilling base and the surface of the base body. Other characteristics that can be determined based on the previously mentioned parameters are the area A_S occupied by the structures and the structural density ρ_S, defined as the ratio of A_S to the total area A_G. For the hexagonal unit cell, ρ_S is calculated as the ratio of the surface areas of a circle and a regular hexagon as follows:

$$\rho_S = \frac{\pi \ d_S^2}{2\sqrt{3} \ a_S^2}. \tag{1}$$

Here, the condition $d_S \leq a_S$ must be satisfied.

For a square arrangement, however, the structural density is calculated by the ratio of the surface areas of a circle and a square with:

$$\rho_S = \frac{\pi \ d_S^2}{4 \ a_S^2}. \tag{2}$$

When using pillar-like structures, the following applies:

$$\rho_K = \rho_S, \tag{3}$$

where ρ_K is defined as the ratio of contact area A_K to total area A_G. However, when holes are used as structural elements, the contact area decreases by the area taken up by the structures

$$\rho_K = 1 - \rho_S. \tag{4}$$

As previously explained, the indentations also serve to capture wear particles. Although significant wear is not expected during the relatively short sliding distances in the sintering process, it is possible for entire powder particles to become dislodged from the component. This can occur due to unintended relative movement when the component is placed on the setter plate. Another critical phase is the heating stage of the sintering cycle, prior to the formation of sufficient sintering necks between the powder particles. The heating causes a relative movement between the component and the sintering base due to the thermal expansion and subsequent onset of shrinkage of the component, during which loose powder particles can also be released. Therefore, the gaps or holes in the surface structure should be large enough to accommodate at least the largest occurring powder particle, characterized by the equivalent particle diameter d_P. For dimple structures, this means that they should be at least as large as the particle diameter.

When using cylindrical elevations, the capture of particles occurs in the gaps. The size of these gaps depends on the

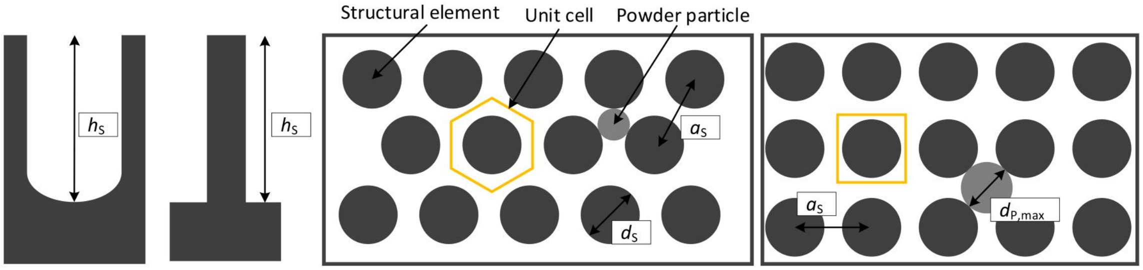

Figure 2. Parameters used to describe the structuring: sectional view of bore and cylinder features (left), top view of a hexagonal arrangement (center), and top view of a square arrangement of structural elements (right).

combination of structural arrangement, element diameter, and spacing. Assuming spherical particles, for a hexagonal arrangement, the particle is located between three structural elements arranged as an equilateral triangle (Fig. 2, center). This results in the maximum particle diameter $d_{P,max}$ being equal to the radius of the triangle's circumcircle minus the radius of the structural elements. For $d_S < a_S$, the diameter $d_{P,max}$ can be calculated as follows:

$$d_{P,\max} = \frac{2}{\sqrt{3}}\ a_S - d_S. \qquad [5]$$

In a square arrangement, the maximum particle diameter $d_{P,max}$ results from the diagonal distance between two structural elements minus the diameter d_S and can therefore be calculated as follows:

$$d_{P,\max} = \sqrt{2}\ a_S - d_S. \qquad [6]$$

Materials and methods

To evaluate the performance of the surface structures, the coefficients of friction at ambient temperatures of 20 °C and 1,100 °C are determined and compared with those of an unstructured reference plate. Dilatometry tests confirm sufficient sintering activity and associated component shrinkage at 1,100 °C, resulting in relative movement between the component and the setter plate.

A custom-built tribometer test rig, as illustrated in Fig. 3 (left), is used in this study. (*3*) The setup includes the LH 30/14 chamber furnace from Nabertherm, which enables precise control of ambient temperature and atmosphere. The measuring system features a linear axis that moves at a constant speed of 0.2 mm/s. This axis drives the specimen, which is placed on a setter plate, via a ceramic rod equipped with an integrated specimen holder. During this movement, the frictional force F_R required to move the specimen is measured by a force sensor located at the opposite end of the rod. The signal is recorded at a sampling rate of 1,000 Hz. In combination with the applied normal force F_N, the static and dynamic friction coefficients are calculated.

The test sequence consists of 32 linear slide-hold-slide cycles. A representative force-displacement curve is shown in Fig. 3 (right). Initially, no load is applied. As the linear axis moves forward, the sensor contacts the ceramic rod, causing the measured frictional force F_R to rise. Once the static friction threshold is reached, the specimen begins to move, transitioning to dynamic friction, which continues until the movement ends. The sensor is then unloaded by a backward movement of the axis, completing the cycle.

The test geometries are square plates with an edge length of 20 mm and a thickness of 4 mm, featuring a radius of 3 mm at the corners, which results in a base area of 392 mm^2. These plates are produced using the DM P2500 system and powder from Digital Metal, with the material being 17-4 PH—a martensitic, age-hardenable steel. The powder has a monomodal particle size distribution, with D10, D50, and D90 values of 7.45, 15.77, and 26.11 µm, respectively. The maximum particle diameter is around 30 µm.

The setter plates consist of aluminum oxide with a purity of ≥99.5% and have a base area of $100 \times 50\ \text{mm}^2$ with a thickness of 2 mm. In terms of roughness, the arithmetical mean height is 1.2 µm and the maximum height is 19.5 µm. Eight different structures were produced by a supplier using laser interference structuring, (*43*) applied to the central area ($30 \times 80\ \text{mm}^2$) of each setter plate. Half of the structures feature depressions, while the other half consists of elevations. The parameters of the structural elements were selected to allow for the investigations of both a wide range of contact surface reduction and the potential to accommodate entire powder particles between or within the structural elements. In addition, the limitations of the manufacturing process had to be considered, which define the minimum feasible size of the structural elements. The achievable structure depth is also constrained by these process limits and reflects the current maximum depth attainable for each respective element size. The following analyses are conducted according to the flow chart illustrated in Fig. 4.

After manufacturing, the characteristics and uniformity of the structures are analyzed on a microscopic level. The aim is to assess the shape deviation of the individual structural elements in relation to the target geometry and to each other. For the assessment, evenly distributed surface areas with a size of approx. $760 \times 570\ \mu\text{m}^2$ are recorded using the 3D laser scanning microscope VK-X3000 from Keyence. Figure 5 (left) schematically shows the position and orientation of the measurement areas on a setter plate. For each structure, 45 images distributed over five rows and nine columns are recorded and analyzed.

The peak material volume V_{mp} and the dale void volume of the valleys V_{vv} are used as evaluation criteria, (*44*) the determination of which is illustrated in Fig. 5 (right) using the material ratio curve. These parameters quantify the extent of reduced peaks and valleys based on volume

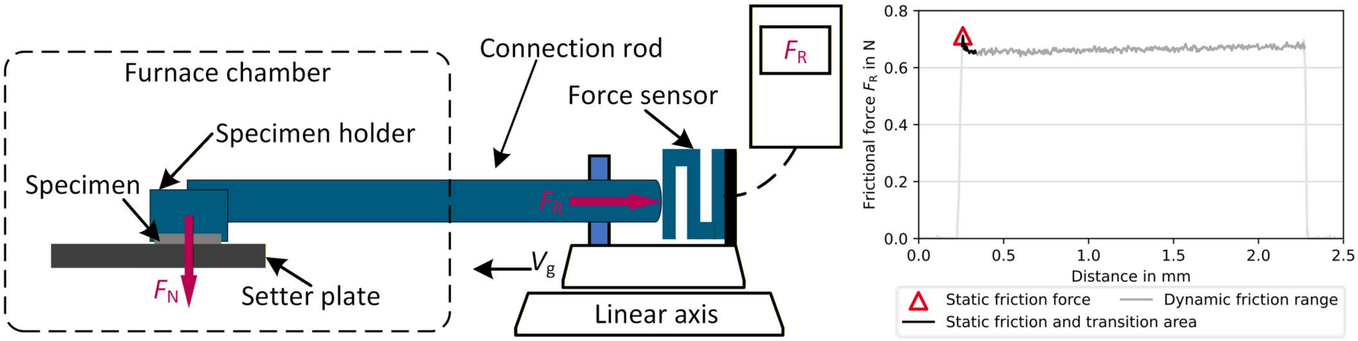

Figure 3. Principle sketch of the measurement setup for determining the friction coefficients under sintering conditions (left) and exemplary measuring signal of a test cycle as force-displacement curve at 20 °C ambient temperature (right). (*3*)

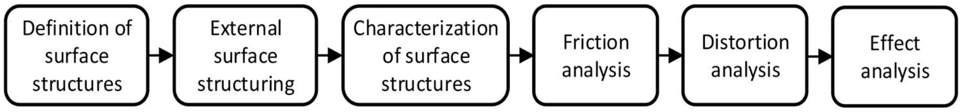

Figure 4. Flowchart of the experimental procedure.

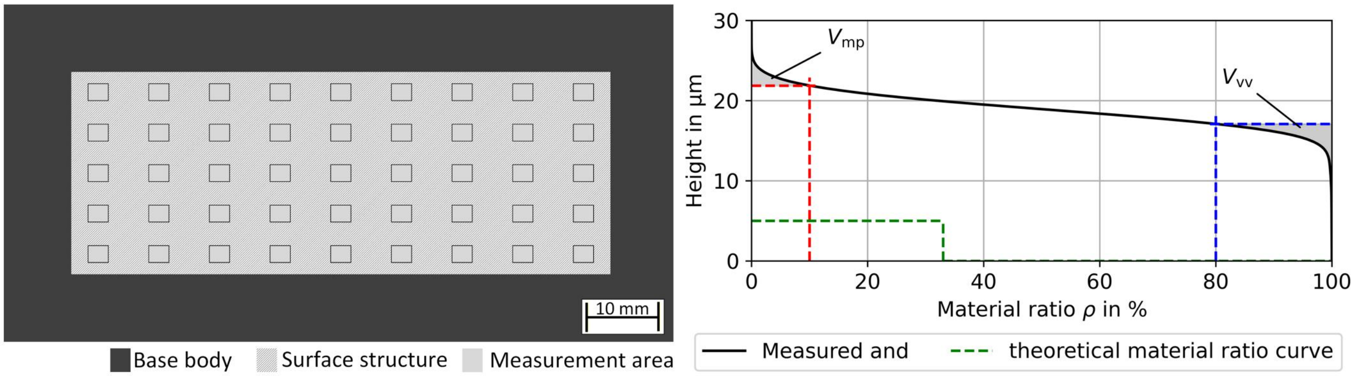

Figure 5. Schematic representation of the structured surface region and the measurement areas on the base body for analyzing the structural elements (left) and illustration of the procedure for determining the surface parameters V_{mp} (peak material volume) and V_{vv} (dale void volume) using the material ratio curve, using surface structure P7 as an example (right).

measurements. The closer the measured material ratio curve aligns with the theoretical one, the more the values of V_{mp} and V_{vv} approach zero. The parameter V_{mp} is used to evaluate pillar structures, while V_{vv} is applied to dimple structures. The material ratio thresholds used for evaluation are selected in accordance with the standard ISO 25178-3. (*45*)

After surface evaluation, the structures are analyzed with respect to their influence on the coefficients of friction. The analysis is first conducted at room temperature, followed by testing at an elevated temperature of 1,100 °C. To ensure a comparable microstructure of the powder particles in both test conditions, the specimens for room temperature testing undergo heat treatment. They are heated at a rate of 3 °C/min to 1,100 °C and cooled down inside the furnace after one-minute holding time. This heat treatment is performed using the furnace of the Desktop Metal Studio System.

Subsequently, the effects on component distortion are analyzed using the geometry shown in Fig. 6 (left). The initial length and width are 20 mm with a height of 15 mm. This geometry is specifically designed to promote significant distortion during sintering, caused by friction between the component and the setter plate (Fig. 6, center and right). The parts are produced using the previously described process chain and sintered on the structured surfaces. The sintering process is carried out using the furnace of the Desktop Metal Studio System. As a measure of distortion, the resulting component width b_{sinter} in the contact plane between the component and the setter plate after sintering is evaluated (Fig. 6, right).

Finally, the effects of the surface structures on the surface quality of the test components and on friction are investigated, along with an analysis of additional potential influencing factors. The factors examined include possible position dependency and the surface topography of the test components. Surface quality is assessed using a laser scanning microscope and includes 24 individual images per component, resulting in six images per contact surface. The total measured area of the composite images is at least $1.5 \times 0.76\,\text{mm}^2$.

For the investigation of position dependency, the temporal progression of friction is analyzed and correlated with the profile of the respective surface structure. To evaluate the influence of specimen surface topography, the heat-treated specimens are ground prior to testing, and then

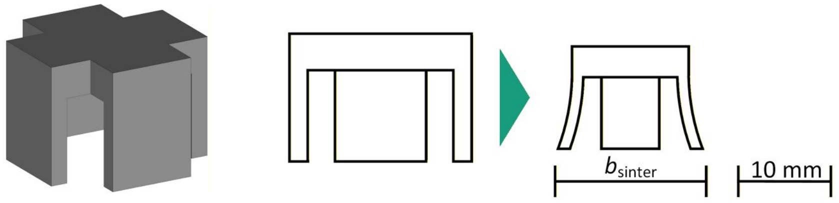

Figure 6. Schematic representation of the test component geometry used to assess component distortion: 3D-view (left), cross-section before sintering (center), and cross-section after sintering (right), including the measured distance b_{sinter} used to quantify distortion.

friction measurements are performed at both room temperature and 1,100 °C.

Results and discussion

Table 1 summarizes the measured parameters of the surface structures examined. A total of eight structures were produced, four featuring pillars and four featuring dimples. The diameters d_S of the structural elements range from 5.0 µm to 44.0 µm, with corresponding heights h_S between 5.0 µm and 100 µm. The spacing a_S between elements varies from 7.7 µm to 80 µm. These dimensions result in structure densities ranging from 21.6% to 45.6%. It should be noted that for the pillar structures, the stated density corresponds to the actual contact area, whereas for the dimple structures, it indicates the percentage reduction in contact area. Consequently, the relative contact area for setter plates with dimple-type structures ranges from 75.8% and 54.4% compared to an unstructured plate. Regarding element spacing, half of the structures allow for the accommodation of entire powder particles. However, the structural depth is not sufficient in all cases. Among the produced surface structures, type P80 provides the greatest available space.

Figure 7 shows three representative topographical images of the P80 and D40 structures. For structure P80 (Fig. 7a and b), the intended cylindrical elements were not formed. Instead, the resulting features exhibit a square cross-section. Nevertheless, the P80 structure shows relatively consistent structural depth and peak heights in some areas (Fig. 7a), while other areas display irregularities (Fig. 7b). In contrast, structure D40, designed as cylindrical holes, exhibits greater variation in peak height (Fig. 7c). Similar deviations are observed in the remaining six structure types: although cylindrical geometries were intended, square-shaped features were produced, and the hole structures show uneven peak heights.

Using the 10% and 80% material ratio values, the distributions of the parameters V_{vv} and V_{mp}, shown in Fig. 8, can be determined. The results indicate that dimple-type structures generally show greater deviations from the ideal geometry compared to pillar-type structures. Among all substrates, structure P7 demonstrates the lowest deviation, with an average peak material volume of 0.11 mL/m^2 and minimal scattering of ±0.01 mL/m^2. In contrast, structure P80 exhibits the highest variation, with a scattering of ±0.31 mL/m^2, attributed to individual outliers. Furthermore, structure D40 shows the greatest deviation from the ideal geometry, with a peak value of 1.06 mL/m^2. Overall, it can be concluded that smaller structures tend to exhibit better conformity with the intended geometry.

Table 1. Measured parameters to characterize the structural elements of the manufactured surface structures.

	Type	d_S (µm)	h_S (µm)	a_S (µm)	$d_{P,max}$(µm)	ρ_S (%)	ρ_K (%)
Dimples	D9	5.0	6.5	9.0	7.7	24.2	75.8
	D21	16.0	20.0	21.0	13.7	45.6	54.4
	D40	24.0	30.0	40.0	32.6	28.3	71.7
	D70	44.0	27.0	70.0	55.0	31.0	69.0
Pillars	P7	5.0	5.0	7.7	5.9	33.1	33.1
	P21	12.0	18.0	21.0	17.7	25.6	25.6
	P40	25.0	27.0	40.0	31.6	30.7	30.7
	P80	42.0	100.0	80.0	71.1	21.6	21.6

The results for the coefficients of friction (Fig. 9) indicate that at 1,100 °C, both static and dynamic friction are consistently higher than at 20 °C, with a more pronounced difference between the two. This increase is assumed to be attributed to plastic deformation at elevated temperatures, which enlarges the real contact area and consequently raises friction levels. (*46*) Additionally, the use of structured surfaces can lead to either an increase or a decrease in the coefficients of friction compared to an unstructured surface. At 1,100 °C, static friction is partially reduced, whereas it tends to increase at room temperature. In both temperature regimes, dynamic friction is higher than the reference value of the unstructured surface. As expected, the static friction coefficient is higher than the dynamic one across all cases. Notably, the static friction values also show greater variability than the dynamic values, particularly at elevated temperatures.

A comparison of the friction measurement data with the structural dimension ρ_K (cf. Table 1) reveals that structures with a significantly lower ratio tend to exhibit reduced static friction. On average, the dimple structures, with contact area ratios ranging from 54.2% to 75.8%, result in an average static friction coefficient of 1.13. In contrast, the pillar structures, with lower ratios between 21.6% and 33.1%, yield an average static friction coefficient of 0.86. Since these differences are only apparent in static friction at 1,100 °C, it is likely that the reduced adhesion caused by the smaller contact area is responsible for this behavior.

Both friction coefficients exhibit a positive correlation (20 °C: $r = 0.997$; 1,100 °C: $r = 0.565$), indicating that an increase in static friction is accompanied by an increase in dynamic friction, and vice versa. However, statistical significance is only evident in the case of dynamic friction. The difference between static and dynamic friction (Fig. 9, right) shows a contrast between testing temperatures of 20 °C and

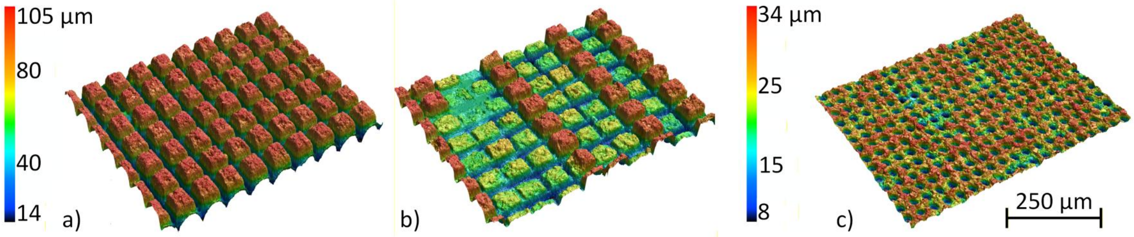

Figure 7. Topographical sections of the surface structures P80 (a, b) and D40 (c).

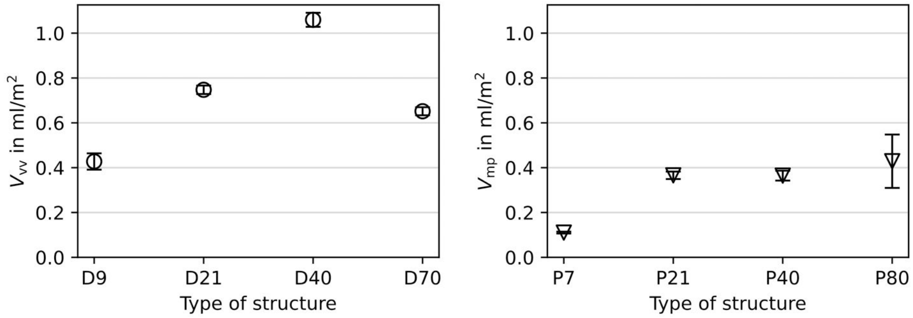

Figure 8. Calculated parameters V_{vv} (left) and V_{mp} (right) for the evaluation of structured surfaces (mean ± 99% confidence interval, number of measurements $n = 45$ per structure).

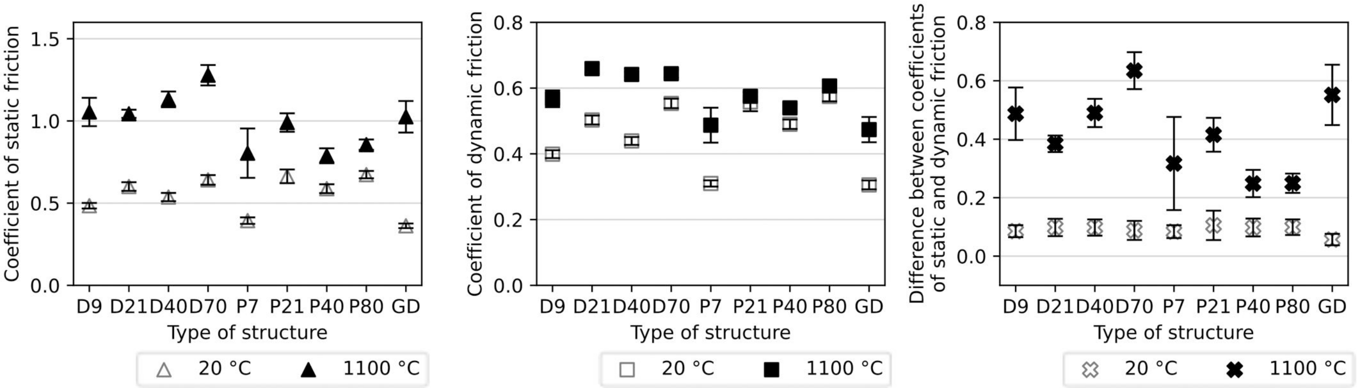

Figure 9. Measured coefficients of static friction (left), dynamic friction (center), and the difference between them (right) for structured and unstructured (GD) setter plates (mean ± 99% confidence interval, number of measurements $n = 30$ per structure).

1,100 °C. At 1,100 °C, the average difference is 0.42, which is more than four times higher than at room temperature. At 20 °C, no significant differences are observed between the various sintering substrates.

When comparing the structures, a qualitative trend is observed between the structural dimensions and the friction coefficients. Larger structures, characterized by the parameters a_S and d_S tend to exhibit higher static and dynamic friction. For example, d_S shows moderate positive correlations with static ($r = 0.68$, $p = 0.063$) and dynamic friction ($r = 0.70$, $p = 0.052$). The spacing a_S showed similar trends (static: $r = 0.68$, $p = 0.065$; dynamic: $r = 0.70$, $p = 0.054$). The height of the structures (h_S) displays slightly weaker correlations (static: $r = 0.58$, $p = 0.136$; dynamic: $r = 0.58$, $p = 0.136$). While there is a general trend that suggests that larger and more spaced structures may increase friction, none of these correlations reached statistical significance in the present dataset, and the differences between static and dynamic friction appear largely unaffected by the tested structural parameters.

At 1,100 °C, all pillar-like structures exhibit lower average friction coefficients compared to the unstructured reference plate, accompanied by a corresponding reduction in the difference between static and dynamic friction for this structure type. In contrast, all dynamic friction coefficients exceed the reference value. Among the dimple structures, D21, D40, and D70 show the highest dynamic friction coefficients, ranging from 0.64 to 0.66, whereas structure P7 shows the lowest value at 0.49. When compared to the average dynamic friction coefficient of the unstructured surface (0.47), this represents an increase of 4% to 40%.

Despite its low peak material volume, structure P7 also exhibits the highest variability in both static and dynamic friction measurements at elevated temperatures. Even at

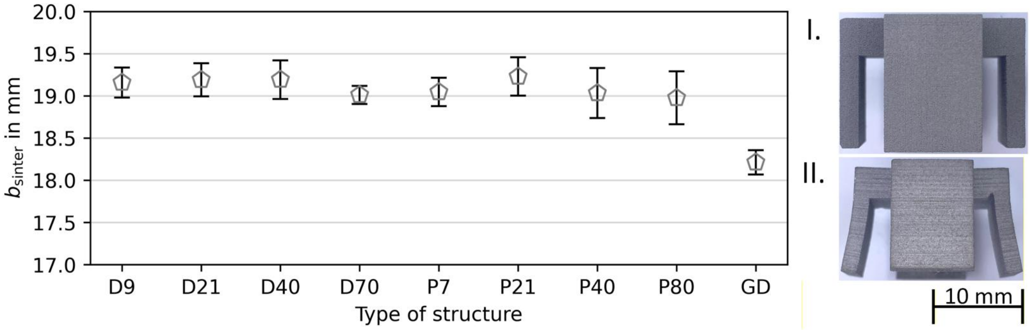

Figure 10. Measured distance b_{sinter} of test components in the contact plane with the substrate after a sintering cycle (mean ± 99% confidence interval, number of measurements $n = 4$ per structure). Additionally shown on the right: side view of the test components before sintering (I) and after sintering on substrate P21 (II).

room temperature, structure P7 results in the smallest increase in friction coefficients: 7% for static friction and 1% for dynamic friction. In contrast, structure P80 produces the largest increase, with static and dynamic friction rising by 86% and 88%, respectively. However, no clear correlation could be established between the friction coefficients and the surface roughness parameters V_{vv} and V_{mp}. Neither the qualitative trends nor the variability or uniformity of the individual structural elements appear to have a significant influence on the measured friction values.

Figure 10 shows the measured width b_{sinter} of the test components in the contact plane after sintering, with four measurements taken per structure type. It can be observed that all test components sintered on structured substrates exhibit a greater final width compared to those sintered on an unstructured substrate. The lowest average width (18.2 mm) was recorded for test components sintered on the unstructured substrate, while those on structured substrates showed an average width of 19.1 mm, which can be attributed to the higher dynamic frictional forces. According to Beere, (*47*) the sintering force is the driving force resulting from the difference in void concentration between pore surfaces and grain boundaries. This force changes throughout the sintering process, approaching zero toward its end. (*48*) If an external force is equal in magnitude to the driving force, no shrinkage occurs. (*49*) Therefore, if a friction force is equal to the driving force, no further shrinkage will occur in the direction of action from this point onwards. However, in other spatial directions or in areas where no frictional force is acting, the component continues to shrink, resulting in non-uniform shrinkage and distortion. If a component is subjected to a higher frictional force, this state of equilibrium will be reached earlier, resulting in less shrinkage or greater geometric deviation. Since shrinkage begins in phase II of the sintering process (*42*) and the width b_{sinter} in the contact plane has already decreased by approx. 1 mm compared to the initial state of the test specimen, it can be assumed that distortion begins during the second heating phase.

Consistent with the friction results, pillar-like structures generally lead to less distortion than dimple-type structures. However, the differences in distortion are small and lie within the 99% confidence interval for the individual structure types. The variance analysis shows that there is a significant difference between structured and unstructured substrates, but not between the different types of structured substrates. A correlation analysis with the friction coefficients at 1,100 °C shows that there is no linear correlation with static friction ($r = 0.027$, $p = 0.944$) and a moderately positive correlation with dynamic friction ($r = 0.608$, $p = 0.082$). While the correlation between increased sliding friction and higher distortion is plausible, it has not yet been statistically proven, but a trend is indicated. This requires a larger number of surface structures. However, it can be assumed that both the increased friction and the higher distortion are due to mechanical interlocking between structures and the rough surfaces of the printed test specimens.

To ensure that the observed differences in b_{sinter} are not caused by variations in the surface roughness of the test components, a roughness analysis is conducted. For this purpose, surface images are captured in the contact plane of each test component. A total of 24 individual images are acquired per surface and compiled into a composite image measuring $1.5 \times 0.76\ \mathrm{mm}^2$. The measurements are carried out under the same conditions as those used for the structural element analyses. The arithmetical mean height S_{a}, the maximum height S_{z}, the reduced valley depth S_{vk}, the reduced peak height S_{pk}, and the core roughness depth S_{k} according to ISO 25178-2 (*44*) are measured. The results are presented in Fig. 11.

Although no valid correlation can be established when using structured substrates, a qualitative trend can be observed. As the roughness parameters increase, the corresponding component width b_{sinter} also tends to increase (ranging from $r = 0.25$ to 0.55 and $p = 0.157$ to 0.546), except for the reduced peak height S_{pk} ($r = -0.20$ and $p = 0.635$). Therefore, these trends are not considered statistically significant.

To assess whether the overall structural quality influences the coefficients of friction, an additional surface profile analysis of the sintering substrates is performed using a Keyence VR-6000 profilometer at 12× magnification. Figure 12 displays an averaged profile line of the P80 structure in the sliding direction. This curve is generated by calculating profile lines at 50 µm intervals across the entire structure and averaging the height values. The corresponding dynamic

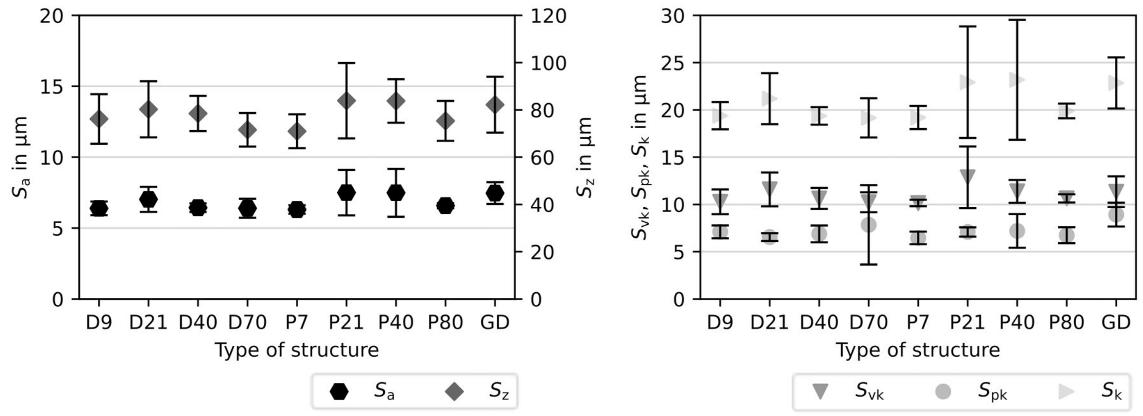

Figure 11. Roughness parameters of the contact surfaces of the test components (mean ± 99% confidence interval, number of measurements $n = 8$ per structure).

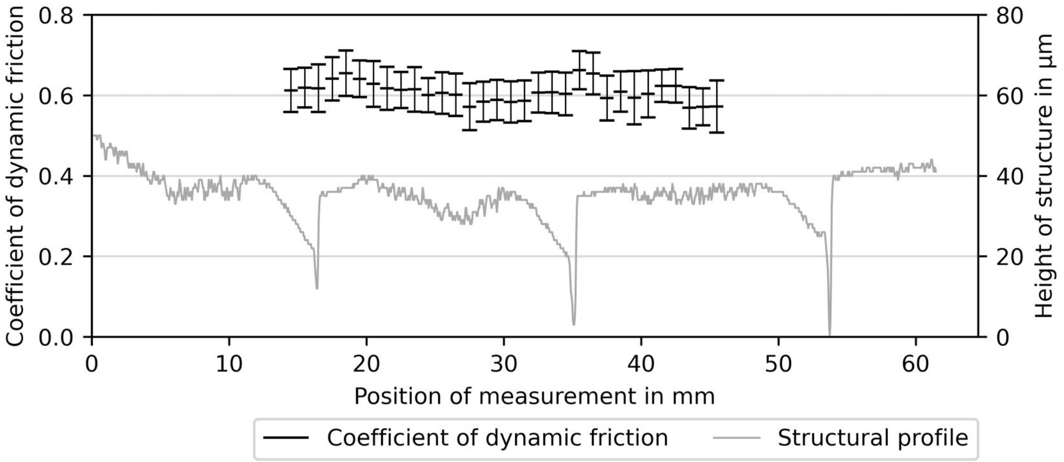

Figure 12. Comparison of the coefficient of dynamic friction at 1,100 °C with the corresponding measurement positions along the averaged surface profile (number of measurements $n = 280$) of structure P80.

friction values and their measurement positions relative to the leading edge of the test specimen are also shown.

The profile reveals three distinct recesses, reaching depths of approx. 40 µm. These recesses result from the segmented manufacturing of the structure, with the depressions corresponding to the overlapping zones between individual segments. Including the spatially resolved dynamic friction values, it can be observed that when the leading edge of the test specimen encounters a pronounced recess, the coefficient of friction increases for approx. 2 mm before subsequently decreasing. At the measurement position of 35 mm, this increase is around 11%. A similar behavior is observed in the other structures as well. Except for structures D9 and P7, the contact between the component edge and the edge of the structure leads to an increase in sliding friction of approximately 11%. The characteristics of these edges and their local height differences are of the same magnitude as those of structure P80. In contrast, structure D9 exhibits a substantially elevated edge height and a locally augmented sliding friction coefficient, reaching approximately 26%. Structure P7, in turn, has no pronounced edges. While the segmented manufacturing of the surface structures does have a measurable influence, the effect is not significant enough to account for the overall differences in friction coefficients or the extent of component distortion due to its short duration. In addition, it has been demonstrated that more pronounced edges result in a more significant increase in local friction.

To further investigate the causes of increased friction and part distortion observed when using structured setter plates compared to unstructured ones, an additional series of experiments is conducted. In this series, ground specimens are used to analyze the influence of surface condition on the friction coefficients. Unlike the smooth components typically referenced in the literature, the printed parts used here exhibit a rougher surface texture, as shown in Fig. 13a and b. This surface texture may promote form-fit interlocking with the structured substrate, potentially leading to increased friction.

For the follow-up experiments, the specimens are presintered and then ground using a wet grinding process. Silicon carbide (SiC) grinding papers with grit sizes P320 and P800 are employed in sequence. The resulting surface is shown in Fig. 13c, while the corresponding roughness parameters are presented in Table 2, compared with those of the previously tested specimens. Surface characterization is carried out using a Keyence VK-X3000 laser scanning microscope. For each specimen, nine images are evaluated,

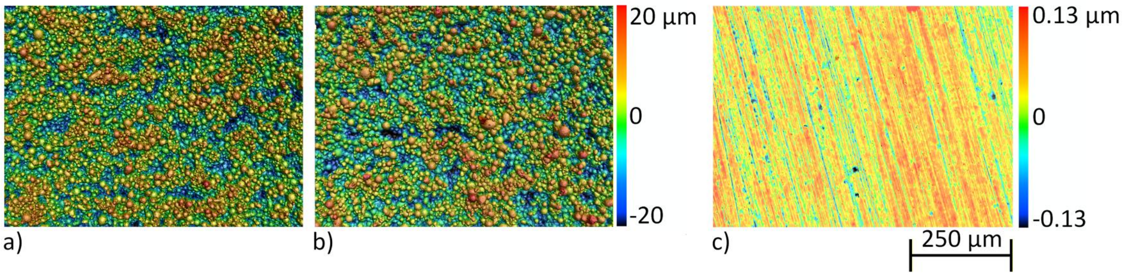

Figure 13. Excerpt of the height profiles of the specimen surfaces in three stages: (a) brown part, (b) pre-sintered state, and (c) ground state.

Table 2. Comparison of surface roughness values of investigated specimens in different conditions.

State	S_a (µm)	S_z (µm)	S_{pk} (µm)	S_k (µm)	S_{vk} (µm)
Brown	6.42 ± 0.54	60.71 ± 5.67	6.11 ± 0.67	20.25 ± 1.48	9.44 ± 1.59
Pre-sintered	6.30 ± 0.40	65.85 ± 5.79	8.15 ± 1.35	19.64 ± 1.29	8.65 ± 1.02
Ground	0.07 ± 0.04	10.20 ± 5.29	0.09 ± 0.09	0.12 ± 0.04	0.30 ± 0.24

each comprising a 3 × 3 composite of individual images with a total size of approx. $570 \times 760\,\mu m^2$. The average roughness values are calculated from these measurements. Imaging is performed at 50× magnification, and an S-filter of 0.8 µm is applied during post-processing.

In contrast to the brown part (Fig. 13a) and the pre-sintered part (Fig. 13b), where powder particles remain clearly visible, the ground surface (Fig. 13c) shows only minor grinding grooves and isolated pores. These pores result from the incomplete sintering process and are not fully closed.

A comparison of the roughness values in Table 2 shows that the two as-built surfaces exhibit no significant differences, while the ground surface displays a drastically reduced surface roughness, as expected. For example, the maximum height S_z is reduced by 85%, and the arithmetical mean height S_a by 99%. Additionally, the reduced peak height S_{pk} is lower not only in absolute terms but also relative to the reduced valley depth S_{vk}, when compared to the as-built surfaces. The lower absolute and relative peak content is expected to have a beneficial effect on the friction coefficients, potentially reducing both static and dynamic friction.

Figure 14 presents the results of the friction analysis for specimens with as-built and ground surfaces at a testing temperature of 20 °C. Compared to as-built specimens, ground surfaces show lower static and dynamic friction coefficients, as well as a smaller difference between the two. While a positive correlation between static and dynamic friction is observed in general, this trend does not apply consistently when comparing the friction profiles of as-built versus ground specimens.

Relative to the as-built specimens, static friction is reduced by 27% to 65%, and dynamic friction by 20% to 64%. The difference between the two is reduced by 60% to 78%. When compared to the unstructured sintering substrate, the use of ground specimens leads to a reduction in static friction of up to 29% and in dynamic friction of up to 34%, both achieved with structure P7. However, in this case, the difference between static and dynamic friction increased by 24%. A reduction in the difference was only observed for structures D9 (17%) and D70 (10%). In contrast, structures P40 and P80 showed increased friction coefficients after surface grinding, with static friction increasing by 8% and 15%, and dynamic friction by 4% and 13%, respectively.

The results for an ambient temperature of 1,100 °C are shown in Fig. 15. In contrast to the findings at room temperature, grinding of the specimens leads to a consistent and, in some cases, pronounced reduction in static friction only. On average, the dynamic friction coefficient remains unchanged showing slight increases in some cases, slight decreases in others, or remaining nearly constant. For example, ground specimens of structures D9 and P7 exhibit a 22% increase in dynamic friction, whereas a 16% reduction is observed for structure D40.

Except for structure P80, the use of structured sintering substrates results in a notable reduction in the difference between static and dynamic friction. While the roughness characteristics of the ground surfaces differ qualitatively between room temperature and 1,100 °C, the trend remains that pillar-like structures exhibit lower average dynamic friction than dimple-like structures.

The prevailing hypothesis suggests that the increase in friction at elevated temperatures can be primarily attributed to two main factors: an increase in the actual contact area due to plastic deformation at the contact surface, and the presence of a visible oxide layer on the components. This observation is consistent with the results of previous tests conducted at elevated temperatures. While the effects on the roughness of the as-built specimens from earlier tests are negligible (Table 2, top line), they lead to a significant increase in roughness in the case of the ground surfaces (Table 3). The values for the pre-sintered specimens (Table 2, center line) are in a similar range, but with considerably lower standard deviations. This is due to the uneven formation of the oxide layer. While the oxide layer is most pronounced along the periphery of the specimen, it decreases continuously toward the center (Fig. 16, right). This can be explained by the limited availability of oxygen in the central area of the specimen. The general formation of the oxide layer results from an insufficiently inert atmosphere within the furnace of the test setup. This is due to the fact that the furnace currently in use is not a conventional sintering furnace, but rather a heat treatment furnace that has been modified with additional apertures for the purpose of integrating measuring equipment. As shown in Fig. 16 (left), this phenomenon does not occur under standard sintering conditions.

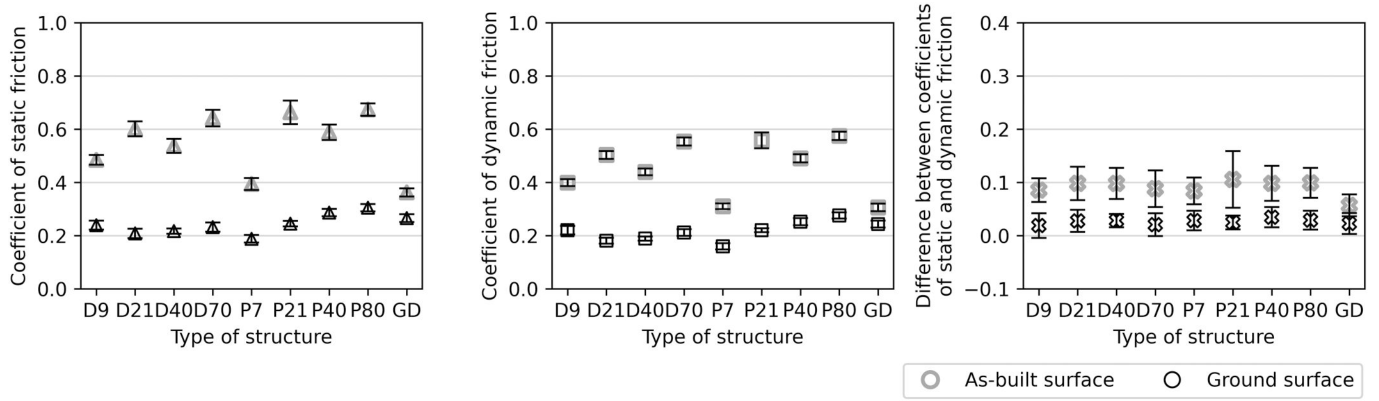

Figure 14. Comparison of the coefficients of friction between ground and as-built specimens using structured substrates at 20 °C (mean ± 99% confidence interval, number of measurements $n = 30$ per structure).

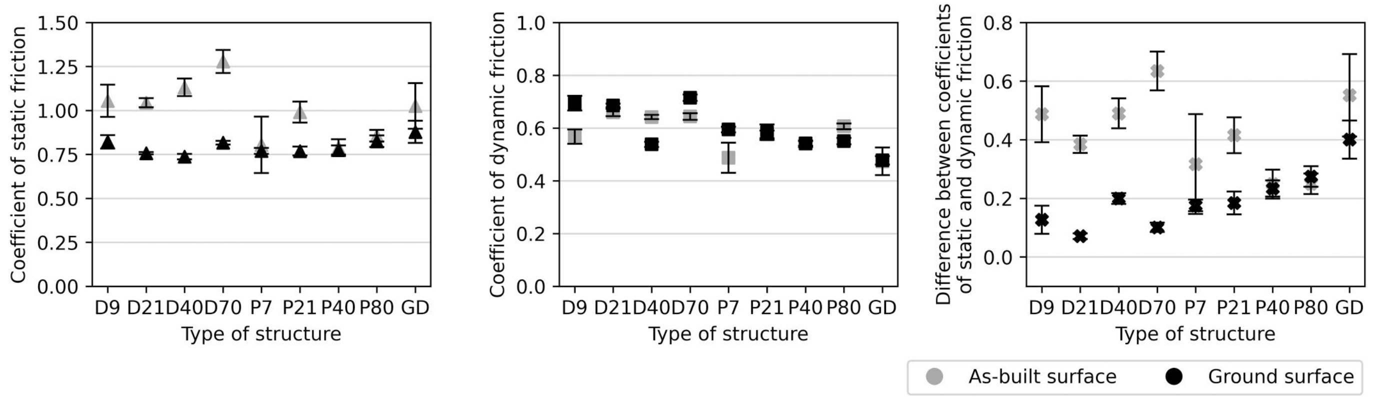

Figure 15. Comparison of the coefficients of friction between ground and as-built specimens using structured substrates at 1,100 °C (mean ± 99% confidence interval, number of measurements $n = 30$ per structure).

Table 3. Roughness values for the oxidized contact surface of the ground specimen.

	S_z	S_a	S_{pk}	S_k	S_{vk}
Mean value (μm)	58.1	6.7	12.4	19.1	5.9
Standard deviation (μm)	20.2	3.8	7.2	12.1	4.6

Figure 16. Comparison of specimen contact surfaces pre-sintered in a protective atmosphere (left) and after grinding under argon atmosphere (right), both at 1,100 °C.

The absence of a friction-reducing effect in the as-built specimens is assumed to be attributed to the fact that the generated surface structuring of the setter plates is likely not fine enough, allowing individual particles on the specimen surface to form a form-fit connection with the surface structure. This mechanical interlocking is illustrated schematically in Fig. 17 (left). A significantly finer surface structuring would ensure that the surface particles of the specimens remain on top of the structural elements, which might then enable a reduction in friction. This also explains why the component distortions are significantly higher for components sintered on structured substrates than on the reference substrate.

Conclusion

This study set out to clarify whether deliberately micro-textured Al_2O_3 setter plates can mitigate the friction induced distortion that MBJ parts experience while shrinking during sintering. Eight textures, four pillar type and four dimple type, were manufactured by laser-interference structuring and tested at ambient temperatures of 20 °C and 1,100 °C. Pillar arrays with contact area ratios down to 22% lowered static friction by as much as 34% at room temperature and by up to 18% at 1,100 °C using ground specimens. Dimple textures, whose contact area ratios exceeded 54%, reduced adhesion only marginally and, in some cases, even increased dynamic friction. Across all structures, there is a general trend that larger structures lead to higher coefficients of friction. A systematic comparison between as-printed and ground specimens revealed that the native, particle-dominated roughness of MBJ parts can dominate the contact mechanics. When the surface is left in its as-printed state,

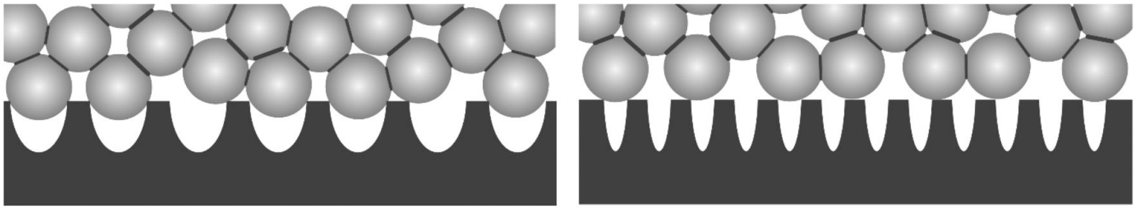

Figure 17. Schematic representation of the interaction between a partially sintered component surface with initial sintering necks between the powder particles and a surface structure with coarse structural elements (left) and fine structural elements (right).

asperities interlock with the texture and largely suppress any friction-reducing effect. A simple two-step wet grind restores the benefit. In addition, all elevated-temperature tests displayed a general upward shift of both static and dynamic friction, which can be attributed to plastic deformation of the metal surface combined with the growth of a thin oxide layer.

Three main constraints of the present study must be acknowledged. First, the chamber furnace used for the in-situ tests could not be fully purged of oxygen. The resulting oxide layer increased surface roughness and rendered the 1,100 °C friction readings upper-bound values. Second, the laser-interference process limited the feature depth ($<100\,\mu m$) and the minimum lateral dimension ($\sim 5\,\mu m$), precluding the evaluation of ultra-fine or markedly deeper textures that might lead to a reduction in friction when using as-printed surfaces. Third, only one material pairing (17-4 PH steel against Al_2O_3) and the MBJ process were investigated; therefore, the generality of the findings for other alloys, setter materials, or processes remains to be proven.

Future work will therefore focus on rerunning the high-temperature tests in a fully oxygen-controlled furnace and documenting any oxide scale that develops by profilometry. It will then move on to producing much finer ($<5\,\mu m$) textures with markedly larger aspect ratios of depth and width, using laser-induced periodic surface structures (LIPSS) (*50*) to broaden the attainable contact area range. At the same time, work is in progress to improve the uniformity of the structures at the microscopic and macroscopic levels. This will clarify how texture depth and local bending stiffness affect friction. Finally, the study will be expanded to include additional alloy–setter pairings and manufacturing processes for producing green parts. This will be supported by finite-element contact simulations. Taken together, these steps should yield setter plates with substantially lower friction, less component distortion, and greater usefulness across the full spectrum of sinter-based manufacturing processes.

Statements and declarations

The authors are co-inventors on a patent application related to the method described in this manuscript.

ORCID

Heiko Blunk http://orcid.org/0000-0001-9861-8236
Arthur Seibel http://orcid.org/0000-0003-3989-9626

References

(1) Munsch, M., Schmidt-Lehr, M., and Wycisk, E. (2018), *Metal Additive Manufacutring with Sinter-Based Technologies*, AMPOWER Insights: Hamburg.

(2) Mostafaei, A., Elliott, A. M., Barnes, J. E., Li, F., Tan, W., Cramer, C. L., Nandwana, P., and Chmielus, M. (2021), "Binder Jet 3D Printing—Process Parameters, Materials, Properties, Modeling, and Challenges," *Progress in Materials Science*, **119**, 100707. doi:10.1016/j.pmatsci.2020.100707

(3) Blunk, H. and Seibel, A. (2025), "Reduction of Sintering Distortion in Metal Binder Jetting: Measuring Friction under Sintering Conditions," *Journal of the Japan Society of Powder and Powder Metallurgy*, **72**, pp S1475–S1479. doi:10.2497/jjspm.16P-T7-01

(4) Blunk, H. and Seibel, A. (2025), "Reduction of Sintering Distortion in Metal Binder Jetting—A Tribological Approach," *Innovative Product Development by Additive Manufacturing*, pp 149–165, Springer Vieweg: Berlin.

(5) Arslan, A., Masjuki, H. H., Kalam, M. A., Varman, M., Mufti, R. A., Mosarof, M. H., Khuong, L. S., and Quazi, M. M. (2016), "Surface Texture Manufacturing Techniques and Tribological Effect of Surface Texturing on Cutting Tool Performance: A Review," *Critical Reviews in Solid State and Materials Sciences*, **41**, pp 447–481. doi:10.1080/10408436.2016.1186597

(6) Rosenkranz, A., Reinert, L., Gachot, C., and Mücklich, F. (2014), "Alignment and Wear Debris Effects between Laser-Patterned Steel Surfaces under Dry Sliding Conditions," *Wear*, **318**, pp 49–61. doi:10.1016/j.wear.2014.06.016

(7) Borghi, A., Gualtieri, E., Marchetto, D., Moretti, L., and Valeri, S. (2008), "Tribological Effects of Surface Texturing on Nitriding Steel for High-Performance Engine Applications," *Wear*, **265**, pp 1046–1051. doi:10.1016/j.wear.2008.02.011

(8) Wu, Z., Xing, Y., Huang, P., and Liu, L. (2017), "Tribological Properties of Dimple-Textured Titanium Alloys under Dry Sliding Contact," *Surface and Coatings Technology*, **309**, pp 21–28. doi:10.1016/j.surfcoat.2016.11.045

(9) Shimizu, J., Nakayama, T., Watanabe, K., Yamamoto, T., Onuki, T., Ojima, H., and Zhou, L. (2020), "Friction Characteristics of Mechanically Microtextured Metal Surface in Dry Sliding," *Tribology International*, **149**, 105634. doi:10.1016/j.triboint.2019.02.042

(10) Sun, Q., Hu, T., Fan, H., Zhang, Y., and Hu, L. (2015), "Dry Sliding Wear Behavior of TC11 Alloy at 500 °C: Influence of Laser Surface Texturing," *Tribology International*, **92**, pp 136–145. doi:10.1016/j.triboint.2015.06.003

(11) Ripoll, M. R., Simič, R., Brenner, J., and Podgornik, B. (2013), "Friction and Lifetime of Laser Surface–Textured and MoS2-Coated Ti6Al4V under Dry Reciprocating Sliding," *Tribology Letters*, **51**, pp 261–271. doi:10.1007/s11249-013-0170-6

(12) Mao, B., Siddaiah, A., Liao, Y., and Menezes, P. L. (2020), "Laser Surface Texturing and Related Techniques for Enhancing Tribological Performance of Engineering Materials: A Review," *Journal of Manufacturing Processes*, **53**, pp 153–173. doi:10.1016/j.jmapro.2020.02.009

(13) Yu, C., Yu, H., Liu, G., Chen, W., He, B., and Wang, Q. J. (2014), "Understanding Topographic Dependence of Friction

with Micro- and Nano-Grooved Surfaces," *Tribology Letters*, **53**, pp 145–156. doi:10.1007/s11249-013-0252-5

(14) Lu, P., Wood, R. J. K., Gee, M. G., Wang, L., and Pfleging, W. (2018), "A Novel Surface Texture Shape for Directional Friction Control," *Tribology Letters*, **66**, pp 1–13. doi:10.1007/s11249-018-0995-0

(15) He, D., Zheng, S., Pu, J., Zhang, G., and Hu, L. (2015), "Improving Tribological Properties of Titanium Alloys by Combining Laser Surface Texturing and Diamond-Like Carbon Film," *Tribology International*, **82**, pp 20–27. doi:10.1016/j.triboint.2014.09.017

(16) Kümmel, J., Braun, D., Gibmeier, J., Schneider, J., Greiner, C., Schulze, V., and Wanner, A. (2015), "Study on Micro Texturing of Uncoated Cemented Carbide Cutting Tools for Wear Improvement and Built-Up Edge Stabilisation," *Journal of Materials Processing Technology*, **215**, pp 62–70. doi:10.1016/j.jmatprotec.2014.07.032

(17) Voevodin, A. A. and Zabinski, J. S. (2006), "Laser Surface Texturing for Adaptive Solid Lubrication," *Wear*, **261**, pp 1285–1292. doi:10.1016/j.wear.2006.03.013

(18) Kang, M., Park, Y. M., Kim, B. H., and Seo, Y. H. (2015), "Micro- and Nanoscale Surface Texturing Effects on Surface Friction," *Applied Surface Science*, **345**, pp 344–348. doi:10.1016/j.apsusc.2015.03.194

(19) Dunn, A., Wlodarczyk, K. L., Carstensen, J. V., Hansen, E. B., Gabzdyl, J., Harrison, P. M., Shephard, J. D., and Hand, D. P. (2015), "Laser Surface Texturing for High Friction Contacts," *Applied Surface Science*, **357**, pp 2313–2319. doi:10.1016/j.apsusc.2015.09.233

(20) Hu, T., Hu, L., and Ding, Q. (2012), "Effective Solution for the Tribological Problems of Ti-6Al-4V: Combination of Laser Surface Texturing and Solid Lubricant Film," *Surface and Coatings Technology*, **206**, pp 5060–5066. doi:10.1016/j.surfcoat.2012.06.014

(21) Hsu, S. M., Jing, Y., Hua, D., and Zhang, H. (2014), "Friction Reduction Using Discrete Surface Textures: Principle and Design," *Journal of Physics D: Applied Physics*, **47**, 335307. doi:10.1088/0022-3727/47/33/335307

(22) Varenberg, M., Halperin, G., and Etsion, I. (2002), "Different Aspects of the Role of Wear Debris in Fretting Wear," *Wear*, **252**, pp 902–910. doi:10.1016/S0043-1648(02)00044-3

(23) Gualtieri, E., Borghi, A., Calabri, L., Pugno, N., and Valeri, S. (2009), "Increasing Nanohardness and Reducing Friction of Nitride Steel by Laser Surface Texturing," *Tribology International*, **42**, pp 699–705. doi:10.1016/j.triboint.2008.09.008

(24) Kumari, R., Scharnweber, T., Pfleging, W., Besser, H., and Majumdar, J. D. (2015), "Laser Surface Textured Titanium Alloy (Ti–6Al–4V) – Part II – Studies on Bio-Compatibility," *Applied Surface Science*, **357**, pp 750–758. doi:10.1016/j.apsusc.2015.08.255

(25) Kumar, V. and Hutchings, I. (2004), "Reduction of the Sliding Friction of Metals by the Application of Longitudinal or Transverse Ultrasonic Vibration," *Tribology International*, **37**, pp 833–840. doi:10.1016/j.triboint.2004.05.003

(26) Kumar, M., Ranjan, V., and Tyagi, R. (2020), "Effect of Shape, Density, and an Array of Dimples on the Friction and Wear Performance of Laser Textured Bearing Steel under Dry Sliding," *Journal of Materials Engineering and Performance*, **29**, pp 2827–2838. doi:10.1007/s11665-020-04816-8

(27) Mao, B., Siddaiah, A., Menezes, P. L., and Liao, Y. (2018), "Surface Texturing by Indirect Laser Shock Surface Patterning for Manipulated Friction Coefficient," *Journal of Materials Processing Technology*, **257**, pp 227–233. doi:10.1016/j.jmatprotec.2018.02.041

(28) Saeidi, F., Parlinska-Wojtan, M., Hoffmann, P., and Wasmer, K. (2017), "Effects of Laser Surface Texturing on the Wear and Failure Mechanism of Grey Cast Iron Reciprocating against Steel under Starved Lubrication Conditions," *Wear*, **386–387**, pp 29–38. doi:10.1016/j.wear.2017.05.015

(29) He, B., Chen, W., and Jane Wang, Q. (2008), "Surface Texture Effect on Friction of a Microtextured Poly(dimethylsiloxane) (PDMS)," *Tribology Letters*, **31**, pp 187–197. doi:10.1007/s11249-008-9351-0

(30) Yasumaru, N., Miyazaki, K., and Kiuchi, J. (2008), "Control of Tribological Properties of Diamond-Like Carbon Films with Femtosecond-Laser-Induced Nanostructuring," *Applied Surface Science*, **254**, pp 2364–2368. doi:10.1016/j.apsusc.2007.09.037

(31) Vagts, S., Schlattmann, J., Kovalev, A., and Gorb, S. N. (2020), "Structure and Frictional Properties of the Leg Joint of the Beetle *Pachnoda marginata* (Scarabaeidae, Cetoniinae) as an Inspiration for Technical Joints," *Biomimetics (Basel, Switzerland)*, **5**, 14. doi:10.3390/biomimetics5020014

(32) Xing, Y., Deng, J., Feng, X., and Yu, S. (2013), "Effect of Laser Surface Texturing on Si_3N_4/TiC Ceramic Sliding against Steel under Dry Friction," *Materials & Design (1980-2015)*, **52**, pp 234–245. doi:10.1016/j.matdes.2013.05.077

(33) da Silva, W. M., Suarez, M. P., Machado, A. R., and Costa, H. L. (2013), "Effect of Laser Surface Modification on the Micro-Abrasive Wear Resistance of Coated Cemented Carbide Tools," *Wear*, **302**, pp 1230–1240. doi:10.1016/j.wear.2013.01.035

(34) Wu, Z., Deng, J., Zhang, H., Lian, Y., and Zhao, J. (2012), "Tribological Behavior of Textured Cemented Carbide Filled with Solid Lubricants in Dry Sliding with Titanium Alloys," *Wear*, **292–293**, pp 135–143. doi:10.1016/j.wear.2012.05.021

(35) Xing, Y., Deng, J., Wu, Z., and Wu, F. (2017), "High Friction and Low Wear Properties of Laser-Textured Ceramic Surface under Dry Friction," *Optics & Laser Technology*, **93**, pp 24–32. doi:10.1016/j.optlastec.2017.01.032

(36) Gachot, C., Rosenkranz, A., Reinert, L., Ramos-Moore, E., Souza, N., Müser, M. H., and Mücklich, F. (2013), "Dry Friction between Laser-Patterned Surfaces: Role of Alignment, Structural Wavelength and Surface Chemistry," *Tribology Letters*, **49**, pp 193–202. doi:10.1007/s11249-012-0057-y

(37) Segu, D. Z. and Hwan, P. (2015), "Friction Control by Multi-Shape Textured Surface Under Pin-On-Disc Test," *Tribology International*, **91**, pp 111–117. doi:10.1016/j.triboint.2015.06.028

(38) Murzin, S. P. and Balyakin, V. B. (2017), "Microstructuring the Surface of Silicon Carbide Ceramic by Laser Action for Reducing Friction Losses in Rolling Bearings," *Optics & Laser Technology*, **88**, pp 96–98. doi:10.1016/j.optlastec.2016.09.007

(39) Wang, M. (2019), "The Tribological Performance of Engineered Micro-Surface Topography by Picosecond Laser on PEEK," *Industrial Lubrication and Tribology*, **72**, pp 172–179. doi:10.1108/ILT-06-2019-0202

(40) Gachot, C., Rosenkranz, A., Hsu, S. M., and Costa, H. L. (2017), "A Critical Assessment of Surface Texturing for Friction and Wear Improvement," *Wear*, **372–373**, pp 21–41. doi:10.1016/j.wear.2016.11.020

(41) Rosenkranz, A., Costa, H. L., Baykara, M. Z., and Martini, A. (2021), "Synergetic Effects of Surface Texturing and Solid Lubricants to Tailor Friction and Wear – A Review," *Tribology International*, **155**, 106792. doi:10.1016/j.triboint.2020.106792

(42) Blunk, H. and Seibel, A. (2026), "Influence of Temperature and Time on the Friction of Additively Manufactured Green Parts during Sintering," *Journal of Tribology*, **148**, 014203. doi:10.1115/1.4069371

(43) Franke, V., Pätzold, G., Klotzbach, U., and Kuntze, T. (2020), "Beeinflussen von Reibung und Verschleiß durch mikrostrukturierte Oberflächen," *Tribologie und Schmierungstechnik*, **67**, pp 34–40. doi:10.30419/TuS-2020-0016

(44) International Organization for Standardization Geometrical Product Specifications (GPS) – Surface Texture: Areal – Part 2: Terms, Definitions and Surface Texture Parameters (ISO 25178-2) (2021).

(45) International Organization for Standardization Geometrical Product Specifications (GPS) – Surface Texture: Areal – Part 3: Specification Operators (ISO 25178-3) (2012).

(46) Mozgovoy, S., Hardell, J., Deng, L., Oldenburg, M., and Prakash, B. (2014), "Effect of Temperature on Friction and Wear of Prehardened Tool Steel during Sliding against 22MnB5 Steel," *Tribology—Materials, Surfaces & Interfaces*, **8**, pp 65–73. doi:10.1179/1751584X13Y.0000000056

(47) Beere, W. (1975), "The Second Stage Sintering Kinetics of Powder Compacts," *Acta Metallurgica*, **23**, pp 139–145. doi:10.1016/0001-6160(75)90079-6

(48) Wakai, F. and Aldinger, F. (2004), "Sintering Forces in Equilibrium and Non-Equilibrium States during Sintering of Two Particles," *Science and Technology of Advanced Materials*, **5**, pp 521–525. doi:10.1016/j.stam.2004.01.018

(49) Gregg, R. A. and Rhines, F. N. (1973), "Surface Tension and the Sintering Force in Copper," *Metallurgical Transactions*, **4**, pp 1365–1374. doi:10.1007/BF02644534

(50) Simões, J., Riva, R., and Miyakawa, W. (2018), "High-Speed Laser-Induced Periodic Surface Structures (LIPSS) Generation on Stainless Steel Surface Using a Nanosecond Pulsed Laser," *Surface and Coatings Technology*, **344**, pp 423–432. doi:10.1016/j.surfcoat.2018.03.052